Empirical Green's Function Retrieval using Cross-correlation of Ambient Noise Correlations (C^2)

Yunfeng Chen[1], and Erdinc Saygin[1,2]

[1]Deep Earth Imaging, Future Science Platform, CSIRO, Perth, WA, 6151, Australia
[2]Department of Physics, School of Physics, Mathematics and Computing, University of Western Australia, Perth, Western Australia, Australia

Key Points:

- An effective higher-order correlation technique is developed to extract the empirical Green's functions (EGFs) from asynchronous networks.
- Our technique cross-correlates the deterministic wavefield from virtual sources and provides high-quality EGF estimates.
- Seismic tomography using asynchronous EGFs offers new constraints to areas undersampled by conventional ambient noise imaging methods.

Corresponding author: Yunfeng Chen, `yunfeng.chen@csiro.au`

Abstract

Empirical Green's function (EGF) retrieval commonly relies on cross-correlating the long-term ambient seismic wavefield that is simultaneously recorded at multiple stations. Recent studies have demonstrated observationally that cross-correlating the coda of ambient noise cross-correlation functions (C^3) enables reconstruction of the EGFs, regardless of the operating time of the stations. In this study, we develop a new technique to perform correlation of cross-correlation functions (C^2), thus permitting the reconstruction of asynchronous EGFs. Our approach exploits the deterministic wavefield rather than the diffusive codas that may be affected by incoherent energy under non-ideal (e.g., sparse, noisy and short-duration) network configurations. We demonstrate the robustness of C^2 by retrieving asynchronous EGFs between 1) nearby stations and 2) distant temporary arrays from southern Australia. The accuracy of the EGFs from C^2 are examined by analyzing seismic tomography of Rayleigh wave group velocities and benchmarking them with the results from conventional ambient noise imaging. The additional ray paths from asynchronous C^2 functions provide better illumination of small-scale crustal structures beneath the regional network. In the larger scale example, involving two asynchronous arrays, the implementation of the C^2 method offers new constraints to the sparsely sampled region of the southern Australian offshore. The resulting velocity model agrees well with the independent structural constraints from individual seismic array studies and sedimentary thickness measurements. This study demonstrates that C^2 is a promising tool for integrating transportable arrays deployed at different times and can greatly benefit the effort of improving seismic data coverage and resolution in crustal imaging.

Plain Language Summary

Seismic waves propagating between a pair of stations can be obtained by cross-correlating the long-term random (noisy-looking) signals simultaneously recorded at two stations. Earlier studies have shown that surface waves propagating between two stations, operated at different times (i.e., asynchronous), can also be obtained by cross-correlating the weak-amplitude coda waves trailing the strong surface waves in the correlation function. In this study, we develop a new method that directly utilizes the energetic surface waves, rather than just the codas, to extract the seismic waves between asynchronous stations. This method is more robust than the earlier proposed coda-wave based approach, espe-

cially when dealing with sparse, noisy and short-duration seismic networks. We apply this new method at different length scales from nearby stations to two far apart, separated networks to demonstrate its superior performance to the traditional approach. The new method can greatly improve data sampling and the resolution of seismic image of subsurface structures.

1 Introduction

Seismic interferometry, commonly known as ambient noise cross-correlation in passive seismology, has been widely applied to probe the structure of the Earth's interior at various scales over the past two decades (e.g., Shapiro & Campillo, 2004; Yao et al., 2006; Lin et al., 2007, 2008; Yang et al., 2007; Stehly et al., 2009; Saygin & Kennett, 2012; Kao et al., 2013; Ward et al., 2013; Rawlinson et al., 2014; Porritt et al., 2016). Both experimental and theoretical studies (e.g., Lobkis & Weaver, 2001; Weaver & Lobkis, 2001; Shapiro & Campillo, 2004) have demonstrated that sufficient time-averaging of the cross-correlation of diffuse wavefields recorded at two receivers effectively converge into the interstation empirical Green's function (hereafter EGF) (see Snieder & Larose, 2013; Campillo et al., 2014; Boschi & Weemstra, 2015, for reviews). Conventionally, ambient noise cross-correlation relies on the acquisition of equipartioned seismic wave energy from simultaneously acting sources (Wapenaar et al., 2010), which imposes a temporal constraint that two stations need to operate simultaneously over a period of time. In recent years, methods have been proposed to reconstruct EGFs by cross-correlating the coda of the correlation functions (hereafter C^3) extracted from the ambient noise (e.g., Stehly et al., 2008; Froment et al., 2011; Ma & Beroza, 2012; Sheng et al., 2018). Such an approach has been largely inspired by the earthquake coda interferometry that utilizes scattered wave energy containing coherent information about the elastic response of the Earth (Campillo & Paul, 2003). An underlying assumption of the C^3 approach is that the long-term stacking of correlation functions produces stable, predominantly time-invariant coda waves (Ma & Beroza, 2012), which permits extracting the EGFs between asynchronous stations from the coherent coda energy acquired at different times. The additional ray paths from the asynchronous EGFs enable improvement of the resolution of crustal imaging (Spica et al., 2016; Ansaripour et al., 2019).

Aside from using diffuse wavefields, another branch of seismic interferometry takes advantage of the deterministic signals from controlled (e.g., Schuster et al., 2004; Bakulin

& Calvert, 2006; Schuster, 2009) or earthquake sources (e.g., Curtis et al., 2009, 2012). This method generally integrates the correlation functions over the (known) distributed sources (Wapenaar et al., 2010). An intriguing implementation is source-receiver interferometry (Curtis & Halliday, 2010) that retrieves the EGF between a source-receiver pair using the deterministic energy propagating from/to a set of surrounding receivers. Its application is not restricted to synchronous source-receiver pairs, thus, the virtual seismogram of an earthquake can be constructed on receivers deployed before or after the event, as long as the recordings are made using a few qualified backbone stations (Curtis et al., 2012).

Both the ambient noise coda-wave correlation (i.e., C^3) and source-receiver interferometry techniques provide a form of temporal redatuming, whereby it is possible to reconstruct the EGFs between asynchronous station-station (earthquake) pairs. In this study, we extend beyond these two methods and examine the feasibility of reconstructing EGFs from the deterministic wavefield extracted from ambient noise data. Specifically, we show that reliable EGF estimates are achievable from higher-order correlations that perform the cross-correlation of correlation functions (hereafter C^2) from surrounding virtual sources (i.e., backbone stations). We demonstrate the effectiveness of the C^2 technique using the data collected from two temporary networks deployed in southern Australia, operated five years apart and separated by a distance of approximately 1500 km (Figure 1). We show that the C^2 method can robustly reconstruct the EGFs between nearby asynchronous stations and can easily be scaled up to achieve continental-scale applications involving distant temporary arrays. Benefiting from the asynchronous EGFs, the surface wave travel-time tomography offers new constraints to the southern Australian offshore, a region poorly resolved by conventional ambient-noise based methods.

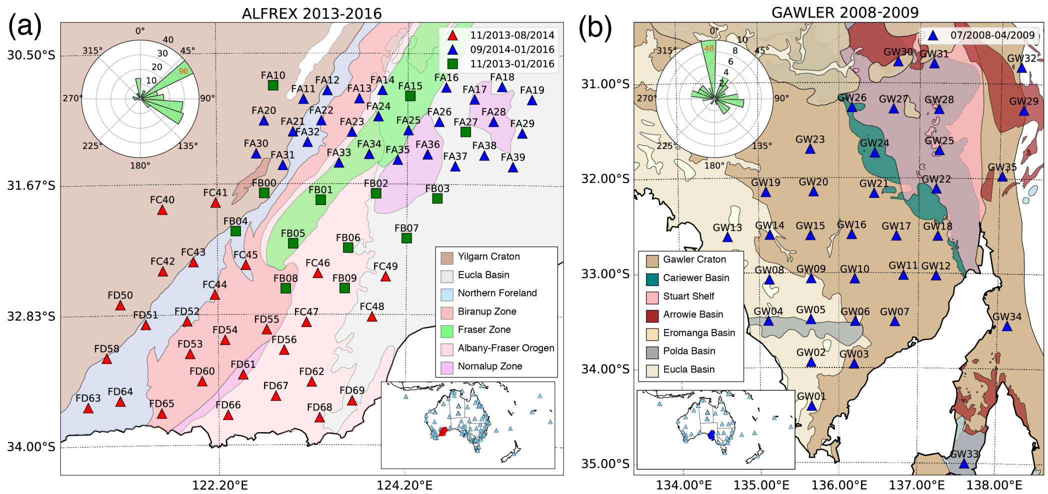

Figure 1. Spatiotemporal distribution of (a) ALFREX and (b) GAWLER seismic networks superimposed on regional geological maps of southern Australia. The crustal domains are colored to show the complex regional tectonic structures. The rose diagram shows the azimuthal distribution of virtual source stations used in the empirical Green's function (C^2) retrieval in the respective test cases. The radial axis is clipped for a better illustration and the number of stations in the dominating direction are labeled on the bar. In the inset map, the locations of permanent seismic stations acting as virtual sources are marked with the cyan triangles and the ALFREX and GALWER networks are highlighted in red and blue.

2 Empirical Green's function retrieval

The computation of C^2 is a two-stage process. The first step of our high-order cross-correlation scheme is to perform the conventional ambient noise cross-correlation (Figure 2a) that is mathematically expressed as

$$G(x, s, t) \simeq u(x, t) \otimes u(s, t), \tag{1}$$

where $G(x, s, t)$ is the EGF between stations x and s at time t, $u(x, t)$ and $u(s, t)$ are the corresponding wavefields recorded at two stations and $\otimes$ represents the cross-correlation operator. This process turns station s into a virtual source (Figure 2b). Although equation (1) does not explicitly differentiate the source types (i.e., diffuse vs. deterministic) in the seismic recordings, ambient noise imaging usually utilizes the stochastic signals (e.g., noise) and removes the contaminating deterministic part (e.g., earthquakes) before cross-correlation (Bensen et al., 2007). Later, we show that this operation is not necessary for extracting EGFs using higher-order cross-correlations. To compute cross-correlation

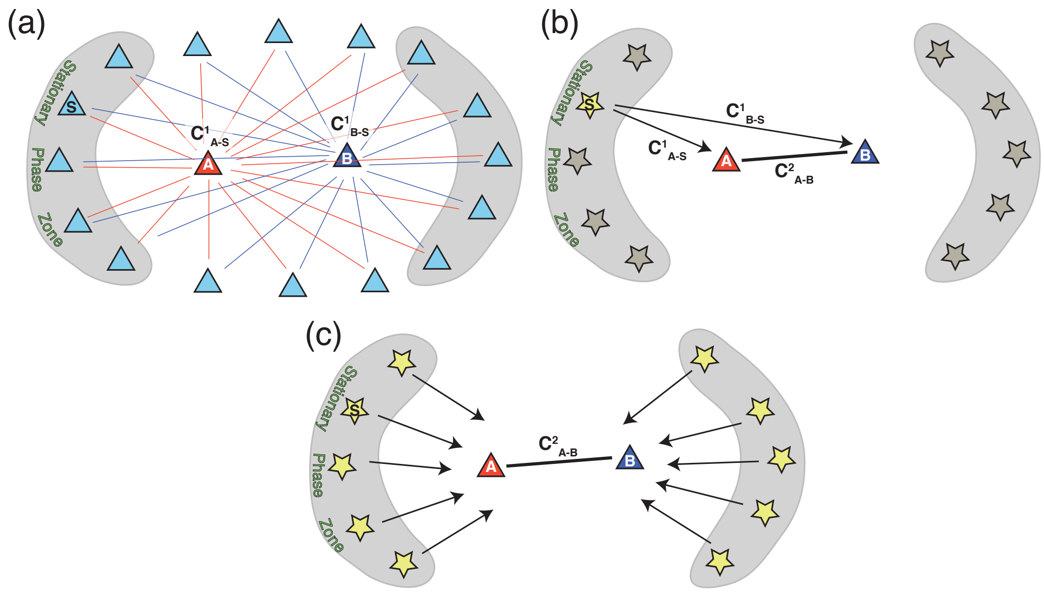

Figure 2. Cartoon illustrates the concept of C^2. (a) Ambient noise correlations are performed between two temporary stations (A and B) and the surrounding permanent stations (S). This process turns the permanent stations into virtual sources. (b) The deterministic surface waves emitted from a virtual source station S (star) are recorded at stations A and B, which are then cross-correlated to obtain a C^2 function. (c) The cross-correlations are conducted for all virtual sources located within the stationary phase zone (shaded grey) that contribute constructively to the stacking.

functions (hereafter C^1) we cut the continuous seismic recordings into one hour segments with a 50% overlap between consecutive windows. After removing the mean and linear trend, we down-sample the data to 5 Hz and apply a bandpass filtering with corner frequencies at 150 sec and 0.5 sec. The processed (synchronous) time series from two stations are cross-correlated and stacked to obtain the final C^1 estimate.

In the second step, we perform EGF retrieval by cross-correlating the correlation functions. This is formulated in the time domain as

$$G(x_B, x_A, t) \simeq \frac{1}{N} \sum_{i=1}^{N} G(x_B, s_i, t) \otimes G(x_A, s_i, t), \tag{2}$$

where $G(x_B, s_i, t)$ and $G(x_A, s_i, t)$ are the EGFs approximated using equation (1) between temporary stations x_A or x_B and a virtual source station s_i , and the summation of correlation functions over N virtual sources produces $G(x_B, x_A, t)$, the EGF between x_A and x_B (Figure 2c). The two temporary stations (i.e., x_A and x_B) need not to be operating at the same time as long as the EGFs from a common virtual source (i.e., s_i) exist, which is typically one of the permanent stations from the backbone seismic network (Figure 1). Therefore, equation (2) provides a framework for reconstructing EGFs between asynchronous stations. In data processing, we select C^1 functions with at least three months of stacking to ensure the signal quality; no prior temporal or frequency normalizations are required. The C^1 functions are divided into causal and acausal signals, and cross-correlation is applied on each segment separately. The resulting two correlation functions (i.e., causal-causal and time reversed acausal-acausal correlations) are stacked to form a C^2 estimate. The final EGF between the two stations is obtained by stacking the normalized C^2 functions from all virtual sources.

3 Data

We apply the proposed higher-order cross-correlation method (C^2) to retrieve EGFs at two length scales 1) asynchronous station pairs within a regional array and 2) two distant temporary networks with different operating periods (see Figure 1). The first example uses the recordings from the ALFREX network that consists of two subarrays, each sampling a part of the Albany-Fraser orogen in southwestern Australia at different time periods, as well as 13 semi-permanent stations operating throughout the acquisition period (Figure 1a). This network configuration is representative of a regional seismic survey with a campaign-mode deployment (e.g., Transportable component of USArray). In

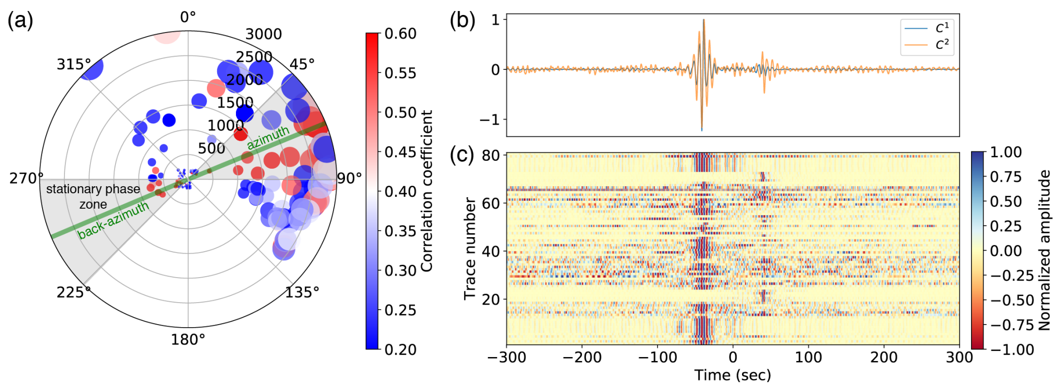

Figure 3. Comparison of the empirical Green's functions retrieved from C^1 and C^2 approaches for the station pair FB07-FB08 within ALFREX. (a) Azimuthal and distance distribution of the correlation coefficient between C^1 and C^2 from individual virtual source. The green line indicates the directions of azimuth and back-azimuth of the selected station pair. The gray shades highlight the stationary phase zone that contributes constructively to the stacking. (b) Waveform comparison between C^1 (orange) and stacked C^2 (blue) using virtual sources within the stationary phase zone. The waveforms are filtered between 2 and 20 sec. (c) Normalized C^2 function from each virtual source contributes to the stack in (b).

the larger scale implementation, we select a distant seismic network (GAWLER) deployed approximately 1500 km to the east of ALFREX near the Gawler craton in southern Australia (Figure 1b). Stations of the GALWER network were operated synchronously between 2008-2009 but did not overlap in time with the ALFREX deployment (2013-2016). The large separation distance and asynchronous operations of the two arrays present great challenges when reconstructing the inter-array EGFs with conventional ambient noise or coda-wave based correlation methods. To implement C^2, we incorporate all the available permanent stations near the Australian continent as virtual sources (see Figure 1).

4 Results

4.1 Empirical Green's function retrieval between asynchronous stations

We compute C^2 between all possible station pairs within the ALFREX network that include both synchronous and asynchronous setups. The synchronous EGFs are extracted between subarrays and 13 semi-permanent stations for a direct comparison with the EGFs obtained from the ambient noise fields (i.e., C^1) (Figure 1a). We show a sample C^2 measurement between a pair of stations located in the center of the ALFREX array to ensure a balanced azimuthal coverage of the virtual sources (Figure 3). We compute the correlation coefficient of C^2 from each virtual source with C^1 as a function of distance and azimuth (Figure 3a). The distribution of the correlation coefficient shows a strong dependence on azimuth: higher values are observed in the directions of azimuth and back-azimuth of the selected station pair, while lower values are distributed perpendicular, consistent with the stationary phase approximation (Snieder, 2004; Snieder et al., 2008). By comparison, the dependency of the correlation coefficient on distance is weak, which may be affected by factors such as site condition, local structures and ambient noise source distributions. We define the stationary phase zone as a 45-degree azimuthal bin centering on the direction of inter-station line and perform stacking of C^2 functions using only virtual sources within this regime. The stacked C^2 is highly consistent with the corresponding C^1 with a correlation coefficient of 0.86 (Figure 3b). Each individual $C^2$from a contributing source shows a clear Rayleigh-type surface wave energy on either a positive or negative time axis, depending on the direction of the source (Figure 3c).

We use stations from several long-operating networks distributed across the Australian continent, which provides approximately 180 virtual sources in C^2 calculation (Figure 4a). The spatial distribution of virtual sources, particularly their azimuthal coverage relative to the temporary stations, strongly affects the quality and reliability of the retrieved EGFs from C^2 (see Figure 3). Thus, we only select the virtual sources that satisfy the stationary phase constraint; on average 50 stations contribute to the stacking of C^2. The resulting EGFs (C^2) show consistent surface wave arrivals characterized by 1) a similar move-out velocity to that of the EGF estimates of C^1 (Figure 4b) and 2) a comparable waveform quality between synchronous and asynchronous station pairs at the overlapped distances (Figure 4c).

4.2 Dispersion measurements and ambient noise tomography

We examine the robustness of the EGFs from C^2 by computing the surface wave dispersion curve. The frequency-dependent Rayleigh wave travel times are determined by FTAN (e.g., Levshin & Ritzwoller, 2001). This method applies a series of narrow-band Gaussian filters with varying center frequencies to the analytical signal of the cross-correlation function. The amplitude of the filtered signal defines an envelope function of the sur-

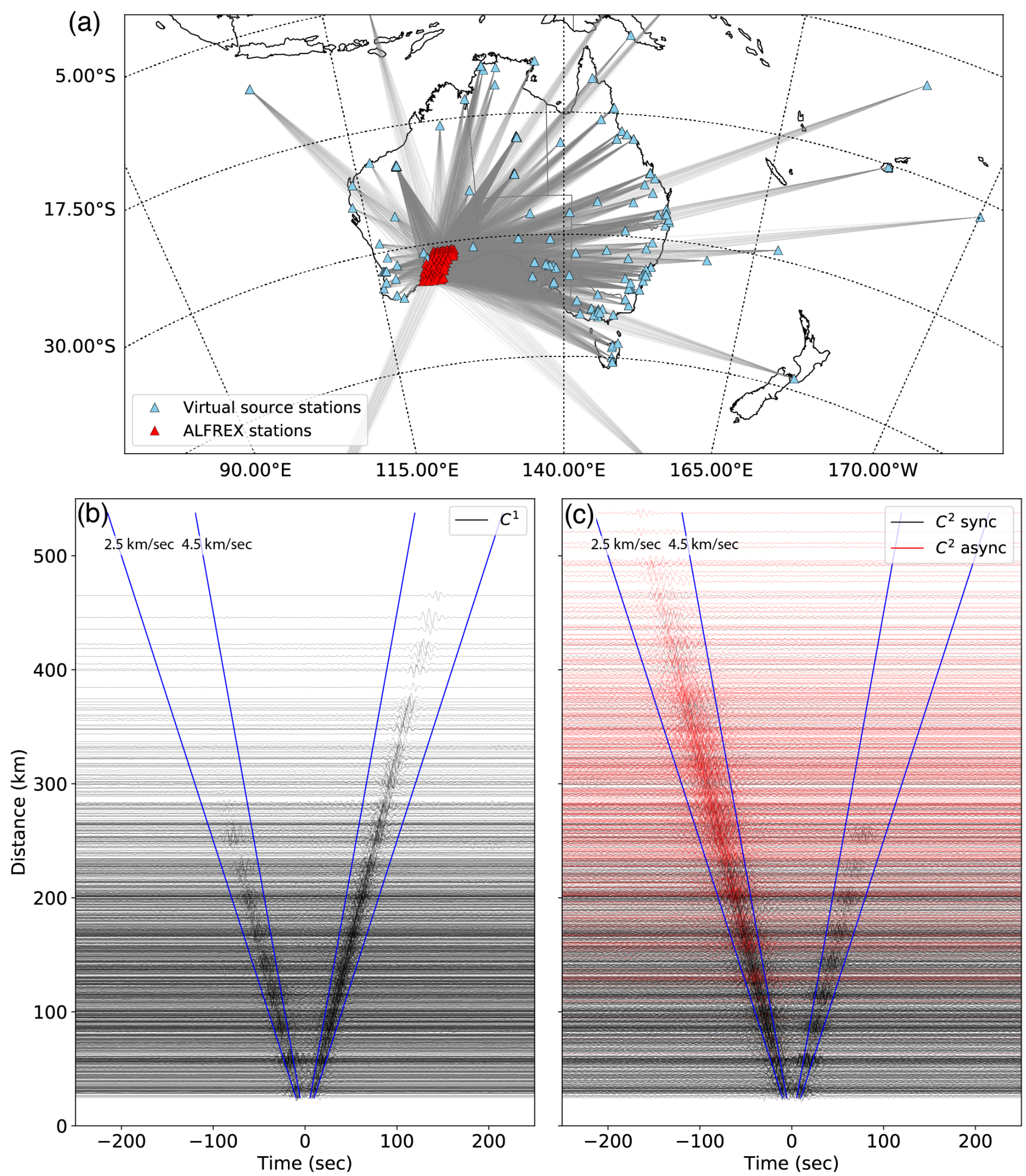

Figure 4. Empirical Green's functions (EGFs) of station pairs within the ALFREX network. (a) The ray-paths between virtual sources (cyan) and ALFREX stations (red) used in calculation of C^2. (b) The EGFs extracted using the C^1 approach. The waveforms are normalized to unity and filtered between 5 and 20 sec. The blue lines mark the respective move-out velocities of 2.5 and 4.5 km/sec, corresponding to the expected range of speed for surface waves in south-western Australia (Saygin & Kennett, 2012). (c) The EGFs between synchronous (black) and asynchronous (red) station pairs from C^2.

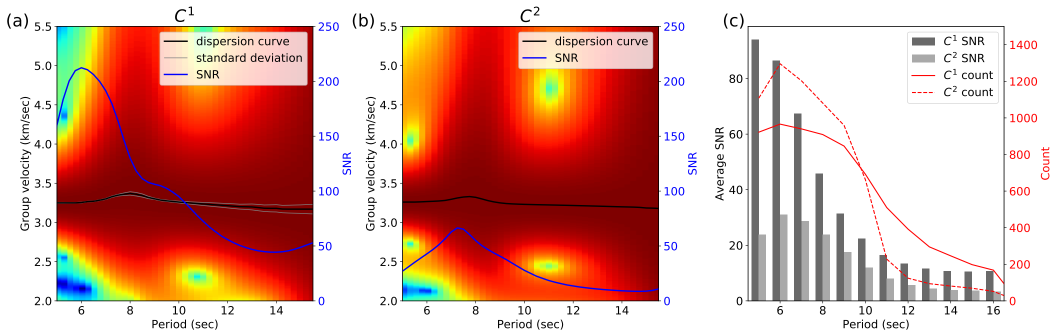

Figure 5. Group velocity measurements of (a) C^1 and (b) synchronous C^2 functions between the station pair FA10-FA15. The black line shows the dispersion curve and the blue line shows the signal-to-noise ratio (SNR) of the cross-correlation function. The uncertainty of the dispersion curve of C^1 is determined by the standard deviation of the measurements on the three-month stacking of C^1 functions (e.g., January-March, February-April etc.). (c) The histogram of average SNR of C^1 (dark grey) and C^2 (light grey) functions at each period. The red solid line shows the number of dispersion measurements of C^1 with SNR>10 and the corresponding result for C^2 is indicated by the dashed line.

face wave, from which the dispersion curve can be retrieved by tracking the peak location of the envelope at each period. The dispersion curves of C^1 and C^2 functions between a sample station pair (FA10-FA15) are highly consistent within the frequency band of interest (4-16 sec) (Figure 5). The average discrepancy is 0.01 km/sec, which is well below the uncertainty range (0.02 km/sec) of the dispersion measurement of C^1 that results from the temporal variation in the EGF (Figures 5a). We further assess the quality of dispersion measurements based on the signal-to-noise ratio (SNR). We define the SNR as the ratio between the maximum absolute amplitude of the surface wave and the standard deviation of the noise in a 500 sec window that starts 500 sec after the surface wave arrival. For the selected station pair, the SNRs of the C^1 and C^2 functions both peak at short periods (7 sec) and decrease rapidly towards longer periods (Figures 5a and 5b). The SNR value of the C^1 function is significantly higher than that of C^2 at all periods, which is expected when C^1 emerges from a sufficiently-averaged ambient noise field. The average SNR of dispersion measurements of all station pairs shows a similar decaying pattern (Figure 5c). For both C^1 and C^2 functions, the majority of high-quality measurements (SNR>10) are concentrated between 5-9 sec, which approximately coincides with the frequency band of the primary microseism (Campillo et al., 2014), and the number decreases with increasing period (Figure 5c). The inclusion of asynchronous station pairs leads to a greater number of measurements of C^2 at periods below 10 sec, beyond which the number decreases quickly to about half of the C^1 results (Figure 5c). The sharp decrease of C^2 measurements at 10 sec is limited mainly by the instrument type of the ALFREX stations, the majority of which are equipped with short-period (1 Hz) sensors. The cross-correlation involving a short-period station produces incoherent signals at longer periods. This effect is amplified in the C^2 function because of the multiple (two-times) cross-correlations of narrow band signals.

4.3 Ambient noise tomography with EGFs from C^2

We perform ambient seismic tomography (ANT) to verify that the EGFs from C^2 are indeed composed of physical signals carrying information on the Earth's structure and are not processing artifacts. We conduct four groups of inversions considering the distinctive ray-path constraints of C^1 and C^2 functions (Figure 6). The C^1 function mainly offers short-distance EGFs between nearby stations (Figure 6a) with the majority of inter-station distances being less than 250 km (see Figure 4b). The C^2 approach enables reconstruction of the EGFs between both synchronous and asynchronous station pairs. The former possesses a similar ray-path coverage to that of C^1 with a slightly lower sampling density (Figure 6b), whereas the asynchronous case provides primarily long-distance (200-450 km) EGFs connecting the two subarrays (Figure 6c). Thus, the combined ray-paths from C^1 and asynchronous C^2 provide complementary (short vs. long wavelength) constraints to the subsurface structures (Figure 6d).

We invert the 5-sec dispersion measurements for group velocities based on an iterative non-linear inversion scheme that applies the fast-matching method for wavefront tracking (Rawlinson & Kennett, 2004). To ensure the accuracy of the dispersion measurement, travel times that deviate largely from the linear trend (i.e., more than two standard deviation) of the time-distance relationship are considered to be outliers and discarded from the subsequent inversion (supplementary Figure S3). The study area is parameterized into a regular grid of 31×31 nodes, which approximates to a cell size of 20 km in both directions. A constant velocity of 3.24 km/sec is assigned to each node location as the initial value. We follow the damping and smoothing criteria from Sippl et al. (2017) for the inversions of C^1, synchronous C^2 and the joint C^1 and asynchronous C^2 functions considering a similar ray-path coverage (Figure 6). Lower values are adopted

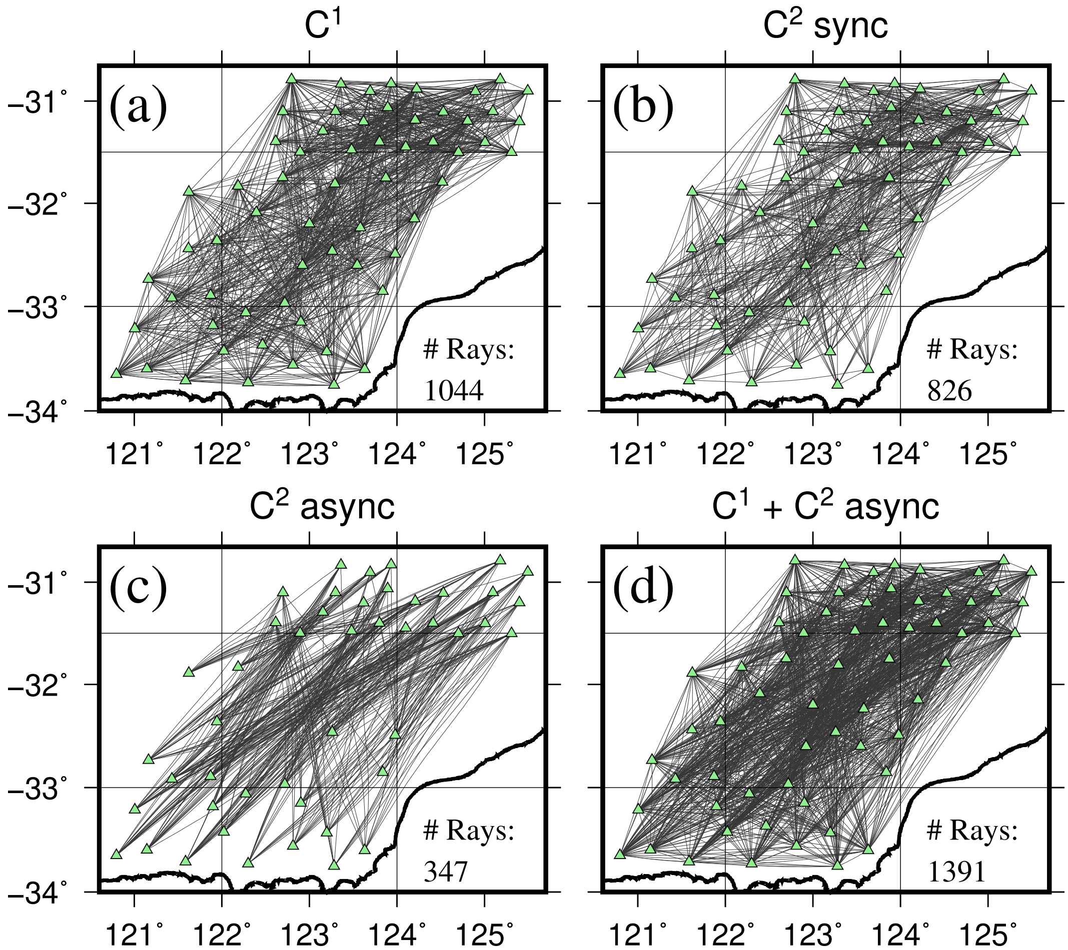

Figure 6. The ray-path coverages at 5 sec of (a) C^1, (b) synchronous C^2, (c) asynchronous C^2 and (d) C^1 and asynchronous C^2 functions from ALFREX. Only ray paths with robust travel-time measurements (i.e., within one standard deviation of the linear regression of time-distance curve) are preserved.

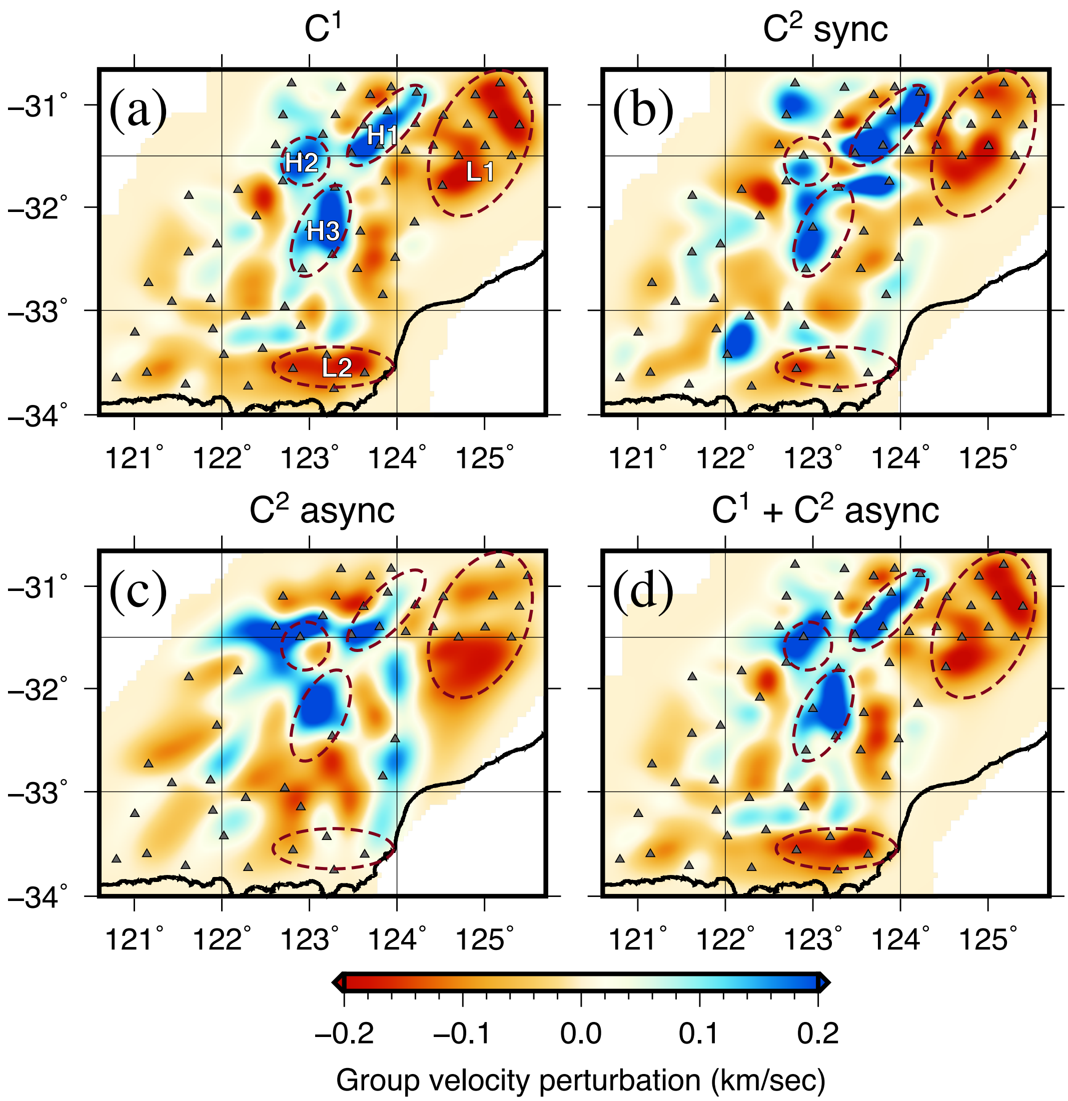

Figure 7. Group velocities at 5 sec beneath the ALFREX network inverted using (a) C^1, (b) synchronous C^2, (c) asynchronous C^2 and (d) C^1 and asynchronous C^2 functions. The velocities are plotted in perturbation relative to the regional mean of 3.24 km/sec. The circled areas highlight the major high (H1-H3) and low (L1-L2) velocity structures discussed in the text.

for the inversion of asynchronous C^2 functions to account for the intrinsic smoothing effect imposed by the long-distance ray-paths (Figure 6c). The resulting C^1 tomogram shows a dominating NE-SW striking high-velocity structure with three distinctive clusters (H1-H3) that are bound by a broad low-velocity zone (L1) to the east and a smaller low-velocity zone (L2) to the south (Figure 7a), consistent with the observations from the study by Sippl et al. (2017). The inversion of synchronous C^2 functions largely confirms the velocity pattern observed in the C^1 result. However, the shape of high-velocity structures (H2 and H3) are less-well constrained and the smaller low-velocity zone (L2) is recovered at a lower amplitude because of reduced ray-path density in these regions (Figure 7b). The asynchronous result successfully captures the large-scale structural variation of the juxtaposed high and low velocities. The recovery of three high-velocity structures is in reasonable agreement with the C^1 result (Figure 7c). The larger low-velocity zone (L1) is generally well resolved, except at the northern tip. In contrast, the smaller-scale low velocity anomaly L2 is characterized by close to average wave speeds, which potentially represents an inversion artifact arising from a lack of crisscrossing ray-paths in that region (Figure 6c). The combined dataset that consists of the C^1 and asynchronous C^2 functions leads to 1) more crisscrossing ray-paths in the center of the network and 2) an increased number of rays sampling the eastern and western flanks of the model (compare Figures 6a and 6d). The overall improvement is subtle as there is a dominating contribution from C^1 functions, yet the resulting model exhibits a better recovery of small-scale anomalies (e.g., H2) and more distinct velocity variation across the array (e.g., shaper contrast between H3 and surrounding regions) (Figure 7d).

4.4 Empirical Green's function retrieval between distant asynchronous networks

The example of ALFREX demonstrates the robustness of the C^2 method in retrieving EGFs within a regional-scale temporary network. A more challenging test is performed on two distant arrays (ALFREX and GAWLER), where the inter-array C^1 is not available because of the non-overlapping deployment periods of the two temporary networks. The dominating east-west orientation of the ray-paths makes the permanent stations located along the eastern and western coasts of Australia the most useful virtual sources for constructing C^2, on average 22 sites contribute to the EGF retrieval (Figure 8a). Despite a significantly smaller number of virtual sources employed in the extractions com-

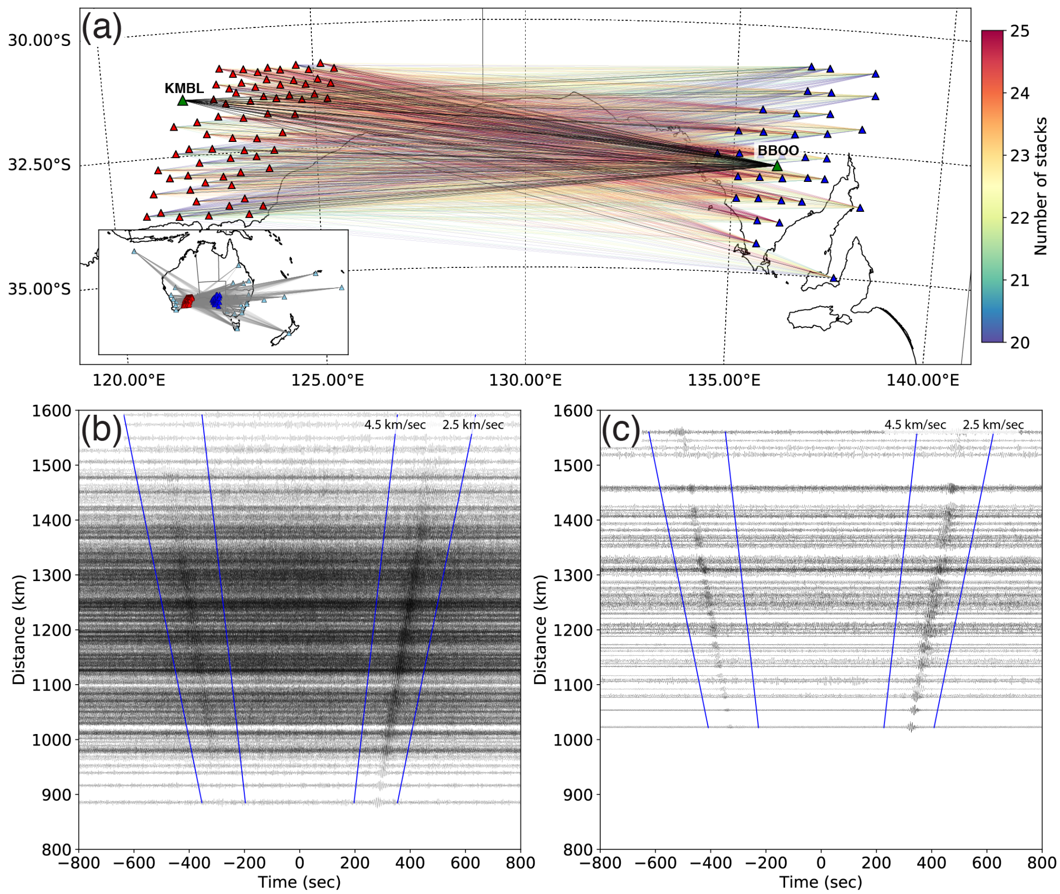

Figure 8. Empirical Green's function (EGF) retrieval using two distant temporary networks of ALFREX and GAWLER. (a) The inter-array ray paths between stations from the two networks color-coded with the number of virtual sources used in the stack. The green triangles mark two nearby permanent stations (KMBL and BBOO) that are used to compute C^1. The ray paths connecting the permanent station to the temporary stations in the opposite network are shown by the black lines. The inset map shows the distribution of virtual source stations (cyan triangles). (b) The inter-array EGFs retrieved using C^2. (c) The EGFs retrieved using C^1 between the selected permanent stations and temporary arrays shown in (a). All waveforms are normalized and filtered between 2 and 20 sec.

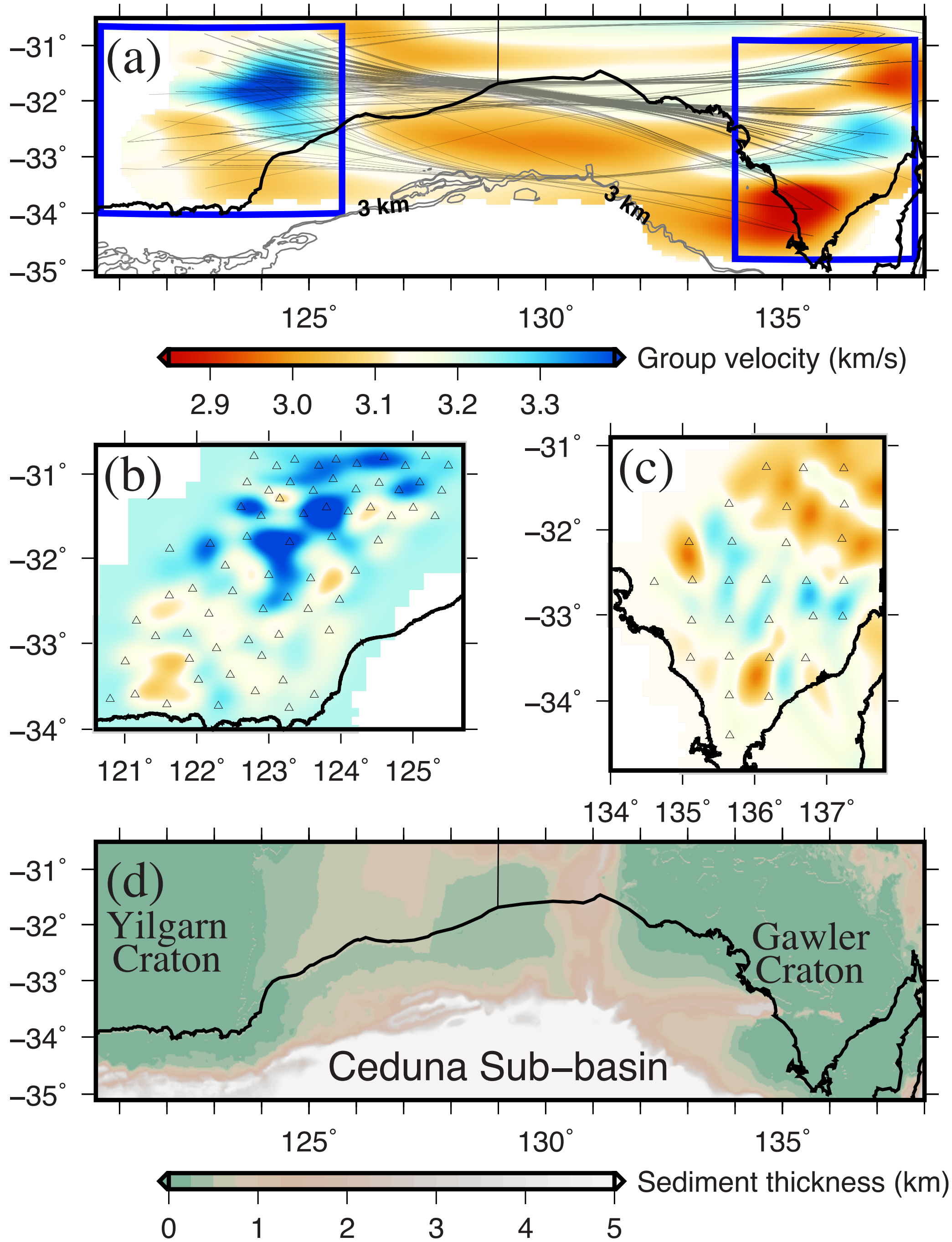

Figure 9. Tomographic inversion using the empirical Green's functions retrieved from C^1 and C^2. (a) The group velocity tomograms at 8 sec constructed by inverting the group delays measured from the EGFs retrieved using C^2 between the two temporary arrays. The locations of ALFREX and GAWLER are highlighted with the blue rectangles. The grey lines indicate the sedimentary thickness contours. The velocities beneath (b) ALFREX and (c) GAWLER inverted using C^1 from the respective arrays. The station locations are indicated by the triangles. (d) The sedimentary thickness distribution near the southern Australian margins obtained from OZ Seebase model (http://www.frogtech.com.au/ozseebase/), providing constraints to shallow crustal structures.

pared to those used in the ALFREX example (see Figure 2b), clear surface wave arrivals can be identified from the resulting C^2 functions (Figure 8b). However, a direct assessment of the quality of inter-array C^2 is prohibited by the lack of C^1 functions from the same ray-paths. Thus, we select two permanent stations in the proximity of the respective temporary networks (Figure 8a) to compute the EGFs using C^1 (Figure 8c). This ensures, as best as possible, a similar spatial sampling to the inter-array area as that of C^2. Benefiting from a long-time (>1 year) averaging of ambient noise, the SNR of C^1 is higher than that of C^2 which has been computed using a limited number of deterministic sources. The consistency between the two sets of EGFs is encouraging in view of 1) a similar move-out velocity of the surface waves and 2) the asymmetric waveforms with a decreasing amplitude at far offsets.

The retrieved EGFs between the ALFREX and GAWLER networks provide new seismic constraints to the subsurface structure of the inter-array area. This broad region marks the complex tectonic setting of the southern Australia continental margin, where the crustal domain transitions rapidly from the Archean Yilgarn craton in the west, through the Proterozoic Albany-Fraser orogen and the Paleozoic offshore basin, to the Archean Gawler craton in the east. Rayleigh wave travel times determined from C^2 functions are inverted with the fast-matching method on a regular grid with 31×31 nodes. The resulting tomogram shows a strong lateral variation from the high group velocities beneath ALFREX and GAWLER networks to a broad intervening low-velocity zone (Figure 9a). The predominantly E-W orientated ray-paths lead to strong smearing, which prevents an accurate assessment of the lateral scale of the size of the velocity structures. In contrast, the nominal resolution in the latitudinal direction is higher, delineating a sharp velocity transition from the continental to offshore areas. The majority of rays propagate along a high-velocity corridor along the continental margin (Figure 9a), a structure that has been reported in an earlier continental-scale model (Saygin & Kennett, 2012). We present independent constraints to the structures beneath the two arrays by inverting the C^1 from the respective network (i.e., intra-array EGFs). The ALFREX result shows a high-velocity zone extending from the center towards the NE (Figure 9b). The structure of GALWER is dominated by a core of scattered high velocities surrounded by reduced wave speeds (Figure 9c). Similar high-velocity structures are revealed by ambient noise imaging using the C^1 technique conducted near the Albany-Fraser orogen (Sippl et al., 2017) and the Gawler craton (Pilia et al., 2015). The spatial distributions and relative strength of the two high-velocity structures beneath the two arrays are highly correlated with those from the tomographic model inverted using the asynchronous EGFs from C^2 (Figure 9a). This broad inter-array region constitutes the offshore of the southern Australian margins that has been sparsely sampled by earlier continental-scale studies (Saygin & Kennett, 2010, 2012). Several offshore basins are covered by a thick Proterozoic-Mesozoic sedimentary sequence, varying from 2 km in the shallow marginal basin to over 15 km in the depocentre of the Ceduna Sub-basin (OZ Seebase model). The propagation of short-period (8 sec) surface waves are mainly sensitive to upper crustal heterogeneities. As a result, the ray-path is strongly affected by the defocusing effect of the low-velocity structures, which generally follow the distribution of shallow (<3 km) sediment deposits in the offshore basins (Figure 9d).

5 Discussion

5.1 Controlling factors for the quality of C^2

The two examples at different scales demonstrate that the EGFs can be robustly retrieved from the deterministic wavefields between asynchronous stations (networks). We discuss a few key factors that can affect the performance of C^2, including 1) the quality of C^1, 2) the azimuthal and distance distribution of the virtual sources and 3) the relative location between a pair of asynchronous stations. Since C^2 exploits the deterministic surface wave energy from C^1, missing or low-quality signals in C^1 inevitably lead to poor EGF retrieval. Specifically, strong noise in C^1 functions often introduces interfering spurious arrivals with amplitudes comparable to that of the surface wave in C^2, which prevents an accurate determination of group/phase arrivals. As has been extensively discussed in earlier studies (e.g., Bensen et al., 2007; Sabra et al., 2005; Stehly et al., 2006; Yang & Ritzwoller, 2008), the quality of C^1 is predominately affected by the spatiotemporal distribution of the noise sources, and a long-term averaging of ambient noises is often required to obtain stable C^1 functions. Signal processing techniques such as Welch's method (Seats et al., 2012) and phase weighted stacking (Schimmel & Paulssen, 1997) can be applied to improve the convergence of C^1 functions.

The dominating factor for obtaining high-quality EGFs using C^2 is the spatial distribution of virtual sources. Unlike C^1 that utilizes ambient noise without well-constrained source locations, C^2 functions are essentially constructed from a set of controlled (virtual) sources that are collocated with the permanent stations (Figure 2). Thus, a biased azimuthal distribution of the virtual sources (see the rose diagram in Figure 1) can preclude a uniform wavefield illumination at the receiver pair of interest, a prerequisite for the constructive stacking of EGFs (Snieder et al., 2008). This criterion is relaxed by the stationary phase approximation, stating that only seismic sources distributed near the inter-station path dominantly contribute to the correct arrival times, hence the constructive stacking of seismic phases (Snieder, 2004; Snieder et al., 2008). In our test cases, the virtual sources that contribute the most to C^2 stacking are spatially confined within a 45-deg bin centering on the line connecting two targeting receivers, whereas non-physical precursory energies emerge when all C^2 functions are stacked without carefully selecting the azimuthal coverage (supplementary Figure S1). An inversion scheme that directly utilizes these biased correlation functions has been recently investigated by Fichtner et al. (2016). Compared to the azimuth, the effect of source-station distance on the quality of individual C^2 is secondary (Figure 3). However, the far-field virtual sources are useful to ensure the constructive stacking of C^2 functions, since the stationary phase approximation is more easily fulfilled by including distant virtual sources, the result of a wider aperture at far distances. Finally, another controlling factor is the relative location between a pair of temporary stations subject to EGFs retrieval. The C^2 achieves the best performance when the majority of virtual sources are well aligned with the targeting station pair. For example, the highest quality EGFs in the AFLREX network are characterized by the dominating NE-SW orientated ray-paths (Figure 6c), consistent with the direction of the densely distributed virtual sources in the NE quadrant (Figure 1a).

5.2 Comparison between C^2 and C^3 methods

In both test cases presented above, the C^3 approach based on cross-correlation of coda waves fails to extract consistent phase arrivals between asynchronous stations (supplementary Figure S2). We attribute the performance difference (C^2 vs. C^3) to the underlying assumptions of the seismic wavefield. The proposed C^2 method exploits the information carried by the deterministic part of the EGF, which is different from C^3 that utilizes the diffuse coda wave energy. The application of C^3 typically succeeds when stable C^1 functions are available from a dense seismic network (e.g., Stehly et al., 2008; Froment et al., 2011; Ma & Beroza, 2012; Zhang & Yang, 2013; Spica et al., 2016, 2017; Sheng et al., 2018). In such cases, the uniformity and diffusivity of the source illuminations of

C^1 can be enhanced through the presence of (near receiver) scatters (Boschi & Weemstra, 2015), which produce a sufficiently diffuse scattering wavefield that is critical for the cancellation of the cross-terms in the correlation functions (Snieder et al., 2008). However, in our study, the C^3 implementation is limited by the incoherent scattering energy in the codas that potentially arises from 1) insufficient recordings from the temporary deployments of networks, 2) a large separation distance between the virtual source and receiver, and/or 3) time-varying and/or a biased distribution of multiple scattering sources. Instead, the C^2 approach utilizes the deterministic energy flux (i.e., surface wave) from a distant source, approximating a plane wave that approaches the two nearby stations at nearly the same angle (azimuth). The accuracy of the travel-time measurements from correlations based on the plane wave assumption has been investigated in earlier studies (Tsai, 2009; Yao & Van Der Hilst, 2009; Boschi et al., 2012) and is also demonstrated by our tomography examples (see Figures 7 and 9). We argue that the C^2 method is less affected by the high-level waveform fluctuations in C^1 codas and is more resistant to network irregularity, such that a few high-quality virtual sources within the stationary phase zone are generally sufficient to provide the unbiased EGF estimates (Figure 3).

5.3 Travel-time bias in EGFs from C^2

Travel-time bias in cross-correlation function resulting from non-isotropic source distribution has been widely reported (e.g., Weaver et al., 2009; Tsai, 2009; Yao & Van Der Hilst, 2009; Froment et al., 2010). The effects of virtual source distribution on travel time are further investigated in our study. The amount of travel-time bias in the C^2 function is determined by the time lag (δt) that leads to the maximum correlation coefficient between the surface waves of C^1 and C^2 functions from the same station pair (Figure 10a) (Froment et al., 2010). To ensure a statistically robust result, we remove large outliers with time lags greater than one standard deviation of the measurements, which typically result from unreliable cross-correlation measurements caused by cycle skipping or noisy C^1/C^2 functions. The cleaned dataset retains 70-90% of the raw measurements, depending on the frequency. The resulting bias is small at shorter periods, which is on par with the sampling rate of the cross-correlation function (0.2 sec), and increases semi-linearly to about 0.5 sec at longer periods (Figure 10b). These travel-time biases are small compared to the total travel times (on average 45 sec) of surface wave, hence only introducing a maximum measurement uncertainty of less than 2%. For most of the mea-

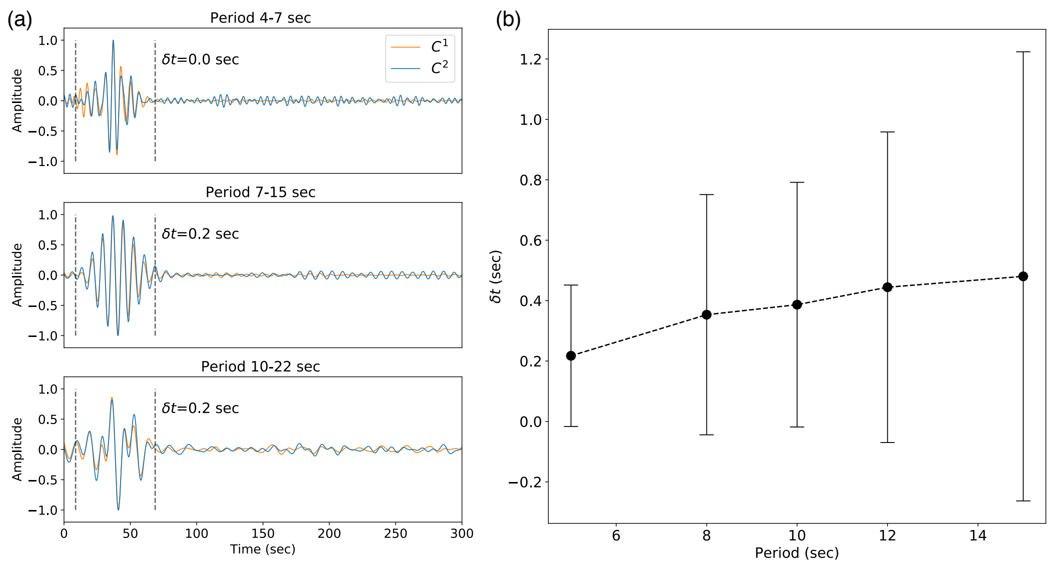

Figure 10. Figure 10 Measurement of the travel-time bias in C^2 functions. (a) A sample measurement for station pair FA30-FB02. The EGFs obtained from C^1 (orange) and C^2 functions (blue) are filtered in multi-frequency bands and their relative travel-time shift (δt) is labeled. The dashed lines indicate the time window of surface wave used in the analysis. (b) Travel-time bias as a function of period for all synchronous station pairs in the ALFREX network. The mean value is marked by the circle and the corresponding standard deviation is indicated by the error bar.

surements, the mismatch between the C^1 and C^2 functions is minimal and excellent consistency exists in surface waves and extends into the late codas (Figure 10a and supplementary Figures S4-S11).

This frequency-dependent uncertainty is consistent with earlier theoretical investigations of the error in apparent travel-time in cross-correlation functions caused by far-field anisotropic sources (Froment et al., 2010; Weaver et al., 2009). These have shown that the predicted travel-time uncertainty decreases at shorter periods and larger inter-station distances. In our study, we do not observe a clear dependency of travel-time bias on distance, which may be caused by a relatively small variation in inter-station distance (~100 km) compared to the length-scale of the far-field sources (in the order of thousands of kilometers; Figure 1). Overall, the effect of non-isotropic wavefield intensity is minimized by stacking the C^2 functions from virtual sources that fall within the stationary phase zone, as validated by our tomographic examples. This non-isotropic effect can be further reduced by the C^3 method that takes advantage of the scattered wavefield (Froment et al., 2010), which may lead to more accurate travel time estimates under an ideal network configuration.

5.4 Relationship to source-receiver interferometry

The representation of C^2 is similar to source-receiver interferometry (Curtis & Halliday, 2010; Curtis et al., 2012) that has been applied to reconstructing the virtual seismograms between earthquake-earthquake (Curtis et al., 2009) or earthquake-station pairs (Curtis et al., 2012; Entwistle et al., 2015). In these implementations, the actual earthquake response is projected to a receiver using the C^1 functions between the target receiver and the backbone stations. The C^2 method differs from source-receiver interferometry by replacing the earthquake with a collocated receiver that acts as a virtual source with respect to the surrounding permanent (backbone) stations. This equivalence also implies a change in source characteristics (depth and focal mechanism) from a complex source-time function of an earthquake to an impulse surface response of the EGF (Denolle et al., 2013). An earlier study extended the applicability of source-receiver interferometry to inter-receiver distances over 2000 km (Entwistle et al., 2015), similar to the length-scale investigated in our study.

6 Conclusion

This study presents the development of a new higher-order cross-correlation scheme (C^2) to extract the EGFs between seismic stations operated asynchronously through deterministic wavefields. Compared to the C^3 approach, the implementation of C^2 is less affected by irregular network configurations and only requires a relatively short recording period of the ambient noise wavefield, hence is ideal for bridging the spatiotemporal gaps between networks deployed at different times. The retrieved EGFs are inverted to obtain group velocities at two length scales, including a regional network with asynchronous station setup and two distant networks operating 5 years apart. The accuracy of the tomographic model derived from the C^2 functions is benchmarked with the results from conventional ambient noise imaging. The larger scale implementation offers new structural constraints to the previously largely undersampled offshore area of southern Australia. We conclude that C^2 is a feasible and promising method for exploiting the information of existing data and improving the resolution of seismic imaging. Our study shows that the current network topology of Australia, characterized by a set of asynchronous transportable arrays covering various parts of the continent and permanent stations mostly deployed along the coastlines, offers an ideal setting to implement the C^2 method. Furthermore, this technique is easily applicable to other continents. With improved data sampling, it is possible to further refine the regional and continental scale crustal models that will ultimately lead to a better understanding of the Earth's structure.

Acknowledgments

We thank the members of Research School of Earth Sciences of the Australian National University for collecting and making the data available. We thank David Howard of GSWA for assistance on ALFREX data. We thank Mehdi Tork Qashqai, Caroline Johnson and Andrew King for reviewing an earlier version of the manuscript. The seismic data used in computing cross-correlation functions are available from IRIS DMC (https://ds.iris.edu/ds/nodes/dmc/) and AusPass (http://auspass.edu.au). Obspy (Beyreuther et al., 2010) and the Generic Mapping Tools (Wessel & Smith, 1998) are used to produce the results.

References

Ansaripour, M., Rezapour, M., & Saygin, E. (2019). Shear wave velocity structure of iranian plateau: Using combination of ambient noise cross-correlations (c1) and correlation of coda of correlations (c3). *Geophysical Journal International*.

Bakulin, A., & Calvert, R. (2006). The virtual source method: Theory and case study. *Geophysics*, *71*(4), SI139–SI150.

Bensen, G., Ritzwoller, M., Barmin, M., Levshin, A., Lin, F., Moschetti, M., ... Yang, Y. (2007). Processing seismic ambient noise data to obtain reliable broad-band surface wave dispersion measurements. *Geophysical Journal International*, *169*(3), 1239–1260.

Beyreuther, M., Barsch, R., Krischer, L., Megies, T., Behr, Y., & Wassermann, J. (2010). Obspy: A python toolbox for seismology. *Seismological Research Letters*, *81*(3), 530–533.

Boschi, L., & Weemstra, C. (2015). Stationary-phase integrals in the cross correlation of ambient noise. *Reviews of Geophysics*, *53*(2), 411–451.

Boschi, L., Weemstra, C., Verbeke, J., Ekström, G., Zunino, A., & Giardini, D. (2012). On measuring surface wave phase velocity from station–station cross-correlation of ambient signal. *Geophysical Journal International*, *192*(1), 346–358.

Campillo, M., & Paul, A. (2003). Long-range correlations in the diffuse seismic coda. *Science*, *299*(5606), 547–549.

Campillo, M., Roux, P., Romanowicz, B., & Dziewonski, A. (2014). Seismic imaging and monitoring with ambient noise correlations. *Treatise on Geophysics*, *1*, 256–271.

Curtis, A., Behr, Y., Entwistle, E., Galetti, E., Townend, J., & Bannister, S. (2012). The benefit of hindsight in observational science: Retrospective seismological observations. *Earth and Planetary Science Letters*, *345*, 212–220.

Curtis, A., & Halliday, D. (2010). Source-receiver wave field interferometry. *Physical Review E*, *81*(4), 046601.

Curtis, A., Nicolson, H., Halliday, D., Trampert, J., & Baptie, B. (2009). Virtual seismometers in the subsurface of the earth from seismic interferometry. *Nature Geoscience*, *2*(10), 700.

Denolle, M., Dunham, E., Prieto, G., & Beroza, G. (2013). Ground motion prediction of realistic earthquake sources using the ambient seismic field. *Journal of Geophysical Research: Solid Earth*, *118*(5), 2102–2118.

Entwistle, E., Curtis, A., Galetti, E., Baptie, B., & Meles, G. (2015). Constructing new seismograms from old earthquakes: Retrospective seismology at multiple length scales. *Journal of Geophysical Research: Solid Earth*, *120*(4), 2466–2490.

Fichtner, A., Stehly, L., Ermert, L., & Boehm, C. (2016). Generalised interferometry-i. theory for inter-station correlations. *Geophysical Journal International*, ggw420.

Froment, B., Campillo, M., & Roux, P. (2011). Reconstructing the green's function through iteration of correlations. *Comptes Rendus Geoscience*, *343*(8-9), 623–632.

Froment, B., Campillo, M., Roux, P., Gouedard, P., Verdel, A., & Weaver, R. L. (2010). Estimation of the effect of nonisotropically distributed energy on the apparent arrival time in correlations. *Geophysics*, *75*(5), SA85–SA93.

Kao, H., Behr, Y., Currie, C. A., Hyndman, R., Townend, J., Lin, F.-C., ... He, J. (2013). Ambient seismic noise tomography of canada and adjacent regions: Part i. crustal structures. *Journal of Geophysical Research: Solid Earth*, *118*(11), 5865–5887.

Levshin, A., & Ritzwoller, M. (2001). Automated detection, extraction, and measurement of regional surface waves. In *Monitoring the comprehensive nuclear-test-ban treaty: Surface waves* (pp. 1531–1545). Springer.

Lin, F.-C., Moschetti, M. P., & Ritzwoller, M. H. (2008). Surface wave tomography of the western united states from ambient seismic noise: Rayleigh and love wave phase velocity maps. *Geophysical Journal International*, *173*(1), 281–298.

Lin, F.-C., Ritzwoller, M. H., Townend, J., Bannister, S., & Savage, M. K. (2007). Ambient noise rayleigh wave tomography of new zealand. *Geophysical Journal International*, *170*(2), 649–666.

Lobkis, O. I., & Weaver, R. L. (2001). On the emergence of the greens function in the correlations of a diffuse field. *The Journal of the Acoustical Society of America*, *110*(6), 3011–3017.

Ma, S., & Beroza, G. C. (2012). Ambient-field green's functions from asynchronous seismic observations. *Geophysical Research Letters*, *39*(6).

Pilia, S., Rawlinson, N., Cayley, R., Bodin, T., Musgrave, R., Reading, A., ...

Young, M. (2015). Evidence of micro-continent entrainment during crustal accretion. *Scientific reports*, *5*, 8218.

Porritt, R. W., Miller, M. S., O'Driscoll, L. J., Harris, C. W., Roosmawati, N., & da Costa, L. T. (2016). Continent–arc collision in the banda arc imaged by ambient noise tomography. *Earth and Planetary Science Letters*, *449*, 246–258.

Rawlinson, N., & Kennett, B. L. (2004). Rapid estimation of relative and absolute delay times across a network by adaptive stacking. *Geophysical Journal International*, *157*(1), 332–340.

Rawlinson, N., Salmon, M., & Kennett, B. L. (2014). Transportable seismic array tomography in southeast australia: Illuminating the transition from proterozoic to phanerozoic lithosphere. *Lithos*, *189*, 65–76.

Sabra, K. G., Gerstoft, P., Roux, P., Kuperman, W., & Fehler, M. C. (2005). Extracting time-domain green's function estimates from ambient seismic noise. *Geophysical Research Letters*, *32*(3).

Saygin, E., & Kennett, B. (2012). Crustal structure of australia from ambient seismic noise tomography. *Journal of Geophysical Research: Solid Earth*, *117*(B1).

Saygin, E., & Kennett, B. L. (2010). Ambient seismic noise tomography of australian continent. *Tectonophysics*, *481*(1-4), 116–125.

Schimmel, M., & Paulssen, H. (1997). Noise reduction and detection of weak, coherent signals through phase-weighted stacks. *Geophysical Journal International*, *130*(2), 497–505.

Schuster, G. (2009). *Seismic interferometry* (Vol. 1). Cambridge University Press Cambridge.

Schuster, G., Yu, J., Sheng, J., & Rickett, J. (2004). Interferometric/daylight seismic imaging. *Geophysical Journal International*, *157*(2), 838–852.

Seats, K. J., Lawrence, J. F., & Prieto, G. A. (2012). Improved ambient noise correlation functions using welch s method. *Geophysical Journal International*, *188*(2), 513–523.

Shapiro, N. M., & Campillo, M. (2004). Emergence of broadband rayleigh waves from correlations of the ambient seismic noise. *Geophysical Research Letters*, *31*(7).

Sheng, Y., Nakata, N., & Beroza, G. C. (2018). On the nature of higher-order ambient seismic field correlations. *Journal of Geophysical Research: Solid Earth*, *123*(9), 7969–7982.

Sippl, C., Kennett, B., Tkalčić, H., Gessner, K., & Spaggiari, C. (2017). Crustal surface wave velocity structure of the east albany-fraser orogen, western australia, from ambient noise recordings. *Geophysical Journal International*, *210*(3), 1641–1651.

Snieder, R. (2004). Extracting the greens function from the correlation of coda waves: A derivation based on stationary phase. *Physical Review E*, *69*(4), 046610.

Snieder, R., & Larose, E. (2013). Extracting earth's elastic wave response from noise measurements. *Annual Review of Earth and Planetary Sciences*, *41*, 183–206.

Snieder, R., Van Wijk, K., Haney, M., & Calvert, R. (2008). Cancellation of spurious arrivals in greens function extraction and the generalized optical theorem. *Physical Review E*, *78*(3), 036606.

Spica, Z., Perton, M., & Beroza, G. C. (2017). Lateral heterogeneity imaged by small-aperture scs retrieval from the ambient seismic field. *Geophysical Research Letters*, *44*(16), 8276–8284.

Spica, Z., Perton, M., Calò, M., Legrand, D., Córdoba-Montiel, F., & Iglesias, A. (2016). 3-d shear wave velocity model of mexico and south us: bridging seismic networks with ambient noise cross-correlations (c1) and correlation of coda of correlations (c3). *Geophysical Journal International*, *206*(3), 1795–1813.

Stehly, L., Campillo, M., Froment, B., & Weaver, R. L. (2008). Reconstructing green's function by correlation of the coda of the correlation (c3) of ambient seismic noise. *Journal of Geophysical Research: Solid Earth*, *113*(B11).

Stehly, L., Campillo, M., & Shapiro, N. (2006). A study of the seismic noise from its long-range correlation properties. *Journal of Geophysical Research: Solid Earth*, *111*(B10).

Stehly, L., Fry, B., Campillo, M., Shapiro, N., Guilbert, J., Boschi, L., & Giardini, D. (2009). Tomography of the alpine region from observations of seismic ambient noise. *Geophysical Journal International*, *178*(1), 338–350.

Tsai, V. C. (2009). On establishing the accuracy of noise tomography travel-time measurements in a realistic medium. *Geophysical Journal International*, *178*(3), 1555–1564.

Wapenaar, K., Draganov, D., Snieder, R., Campman, X., & Verdel, A. (2010). Tutorial on seismic interferometry: Part 1basic principles and applications. *Geophysics*, *75*(5), 75A195–75A209.

Ward, K. M., Porter, R. C., Zandt, G., Beck, S. L., Wagner, L. S., Minaya, E., & Tavera, H. (2013). Ambient noise tomography across the central andes. *Geophysical Journal International*, *194*(3), 1559–1573.

Weaver, R., Froment, B., & Campillo, M. (2009). On the correlation of non-isotropically distributed ballistic scalar diffuse waves. *The Journal of the Acoustical Society of America*, *126*(4), 1817–1826.

Weaver, R., & Lobkis, O. (2001). Ultrasonics without a source: Thermal fluctuation correlations at mhz frequencies. *Physical Review Letters*, *87*(13), 134301.

Wessel, P., & Smith, W. H. (1998). New, improved version of generic mapping tools released. *Eos, Transactions American Geophysical Union*, *79*(47), 579–579.

Yang, Y., & Ritzwoller, M. H. (2008). Characteristics of ambient seismic noise as a source for surface wave tomography. *Geochemistry, Geophysics, Geosystems*, *9*(2).

Yang, Y., Ritzwoller, M. H., Levshin, A. L., & Shapiro, N. M. (2007). Ambient noise rayleigh wave tomography across europe. *Geophysical Journal International*, *168*(1), 259–274.

Yao, H., & Van Der Hilst, R. D. (2009). Analysis of ambient noise energy distribution and phase velocity bias in ambient noise tomography, with application to se tibet. *Geophysical Journal International*, *179*(2), 1113–1132.

Yao, H., van Der Hilst, R. D., & De Hoop, M. V. (2006). Surface-wave array tomography in se tibet from ambient seismic noise and two-station analysisi. phase velocity maps. *Geophysical Journal International*, *166*(2), 732–744.

Zhang, J., & Yang, X. (2013). Extracting surface wave attenuation from seismic noise using correlation of the coda of correlation. *Journal of Geophysical Research: Solid Earth*, *118*(5), 2191–2205.